Research Article | Vol. 10, No. 6 / 1 June 2020 / Optical Materials Express 1451
Optical Materials EXPRESS

Relative oxidation state of the target as guideline for depositing optical quality RF reactive magnetron sputtered Al_2O_3 layers

CARLIJN I. VAN EMMERIK,[1] WARD A. P. M. HENDRIKS,[1] MARTIJN M. STOK,[1] MICHIEL DE GOEDE,[1] LANTIAN CHANG,[1] MEINDERT DIJKSTRA,[1] FRANS SEGERINK,[1] DOMINIC POST,[2] ENRICO G. KEIM,[3] MIKE J. DIKKERS,[3] AND SONIA M. GARCÍA-BLANCO[1,*]

[1] *Optical Sciences group, MESA+ Institute, University of Twente, 7500AE, Enschede, The Netherlands*
[2] *Inorganic Material Sciences group, MESA+ Institute, University of Twente, 7500AE, Enschede, The Netherlands*
[3] *Nanolab, MESA+ Institute, University of Twente, 7500AE, Enschede, The Netherlands*
[*] *s.m.garciablanco@utwente.nl*

Abstract: Amorphous Al_2O_3 is an attractive material for integrated photonics. Its low losses from the UV till the mid-IR together with the possibility of doping with different rare-earth ions permits the realization of active and passive functionalities in the same chip at the wafer level. In this work, the influence of reactive gas flow during deposition on the optical (i.e., refractive index and propagation losses) and material (i.e., structure of the layer) characteristics of the RF reactive sputtered Al_2O_3 layers is investigated and a method based on the oxidation state of the sputtering target is proposed to reproducibly achieve low loss optical guiding layers despite the continuous variation of the condition of the target along its lifetime.

© 2020 Optical Society of America under the terms of the OSA Open Access Publishing Agreement

1. Introduction

Aluminum oxide (Al_2O_3) is a dielectric material commonly used as coating for many applications due to its excellent properties [1], such as high hardness [2,3], durability and wear [4]. Al_2O_3, both in its crystalline [5–7] as well as amorphous phases [8–14], is also an attractive material for integrated photonics. In particular, amorphous Al_2O_3 has a moderate refractive index (n~1.65 at 633 nm [15]), a wide transparency window (150-5500 nm [15,16]) and low propagation losses (i.e., planar waveguide losses of 0.12 ± 0.02 dB/cm have been reported at 1523 nm [17,18]). Amorphous Al_2O_3 exhibits high rare-earth ion solubility in comparison with other materials used in integrated photonics, such as Si and Si_3N_4 [19,20], with moderate luminescence quenching [11,21]. Rare-earth ion doped amorphous aluminum oxide has been used for the realization of waveguide lasers emitting at different wavelengths, including ~0.88, ~1.06 and ~1.330 µm (i.e., Nd^{3+}:Al_2O_3) [22], ~1.03 µm (i.e., Yb^{3+}:Al_2O_3) [23,24], ~1.55 µm (i.e., Er^{3+}:Al_2O_3) [8–10,23,25,26], ~1.8-1.9 µm (Tm^{3+}:Al_2O_3) [27–29] and ~2 µm (Ho^{3+}:Al_2O_3) [12] and amplifiers, operating in the C-band [11,17,19,30,31]. Given its ease of deposition at the wafer-level, Al_2O_3 is well-suited for integration as gain material with the well-established Si_3N_4 [10,31–34] and Si [35–37] integrated photonic platforms.

Al_2O_3 can be deposited using different methods including the synthesis by the sol-gel method [38,39], chemical vapor deposition (CVD) [40], pulsed laser deposition (PLD) [41,42], atomic layer deposition (ALD) [31,43–46] and reactive co-sputtering [15,18,47]. The performance of the devices made by sol-gel and CVD method suffer from luminescence quenching due to OH^- incorporation [48], whereas PLD and ALD are limited by their low growth rate for wafer scale Al_2O_3 layers [42,46]. Reactive magnetron sputtering is suitable for wafer scale deposition. However, DC-powered sputtering suffers from arcing [15], making it difficult to deposit high

#393058 https://doi.org/10.1364/OME.393058
Journal © 2020 Received 17 Mar 2020; revised 7 May 2020; accepted 10 May 2020; published 27 May 2020

optical quality layers. Alternative methods include pulsed-DC sputtering, mid-frequency AC sputtering, high-power impulse magnetron sputtering and RF sputtering. In this work, RF-powered sputtering was utilized. RF sputtering has been previously shown to produce layers with low OH^- incorporation and low optical losses [17–18,25].

The influence of the hysteresis observed on the bias voltage [49–51], on the reactive gas partial pressure [52] and on the deposition rate [53] versus oxygen flow during magnetron sputtering of Al_2O_3 coatings as well as the temperature treatment during and after [54–55] the deposition process have been studied over the last few years and the mechanical characteristics of the resulting Al_2O_3 coatings have been reported. Published results show that the optimal deposition parameters are very dependent on the history of the process and erosion of the target [51,56,57]. However, limited number of studies have been focused on understanding how the deposition parameters affect the optical properties (i.e., refractive index and propagation loss) of the Al_2O_3 layers [15,25,46,47,58,59] and how to select the desired deposition conditions to achieve layers of reproducible optical properties along the lifetime of the target. Demirtas et al. investigated the influence of the deposition temperature on the optical losses of Al_2O_3 layers deposited by ALD [46,47]. Díaz León et al. investigated the influence of pulsed-DC magnetron sputtering with different RF substrate bias without substrate heating on the optical losses of Al_2O_3 layers [47] and Wörhoff et al. presented a comparative study between DC and RF reactive sputtering [15] and their influence on the optical characteristics of the layers. The effect of reactive gas (i.e., oxygen) flow during deposition on the optical properties of the sputtered Al_2O_3 layers and how this parameter should be selected to achieve reproducible sputtered layers along the lifetime of the sputtering target has not yet been systematically studied, although it is known to be a key parameter in reactive magnetron sputtering.

In this work, the influence of oxygen flow on the optical and material characteristics of RF reactive magnetron sputtered Al_2O_3 layers is studied. By proper choice of this parameter, the refractive index, propagation losses and crystallinity of the Al_2O_3 layers can be controlled. Transmission electron microscopy (TEM) and X-ray diffraction (XRD) are used to identify the crystallinity of the layer (i.e., amorphous vs (poly)crystalline). Prism coupling was used to determine the layer thickness and refractive index of the layers and to qualitatively evaluate their propagation losses. The results of this study permit understanding how to select the optimum set-point for the sputter deposition process to achieve the desired optical properties for the layers in a reproducible and stable manner.

2. Experimental methods

An AJA ATC 15000 RF reactive co-sputtering system [15,17,18] is used for the deposition of Al_2O_3 layers (Fig. 1). A 10 cm in diameter silicon wafer with 8 µm thick thermal oxide layer is introduced through a load-lock and it is placed on a rotating heated holder in the main reaction chamber. Three magnetrons, designed for 2-in targets are present in the machine, and currently used for aluminum (Al, 99.9995% purity), erbium (Er, 99.95% purity) and ytterbium (Yb, 99.9% purity). Two targets can be powered with their own RF power source at the same time, although in this work, only undoped Al_2O_3 layers have been studied. The main chamber is pre-evacuated to a base pressure of 0.1 µTorr (i.e., 13 µPa) using a turbomolecular pump. Such a low base pressure is necessary to reduce the OH^- level. OH^- bonds incorporated into the material induce absorption losses from the visible to the near infrared, with the most pronounced overtones of the fundamental absorption in the 700-1600 nm wavelength range [60]. OH^- bonds also produce strong luminescence quenching when the layers are doped with rare-earth ions [41,61].

A power of 200 W is used on the Al-target and an argon flow of 25.0 sccm is utilized. An oxygen flow is added to oxidize the aluminum ions to form an Al_2O_3 layer on the wafer. The oxygen flow needed to obtain optically guiding layers depends on the relative oxidation state of the sputtering target, as it will be explained later, and varies in the range of 2.0-2.8 sccm

Optical Materials EXPRESS

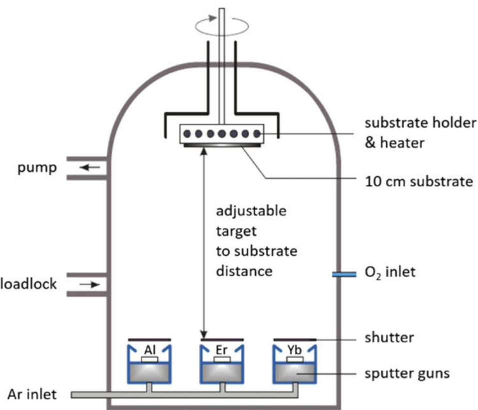

Fig. 1. Schematic of the AJA ATC 15000 RF reactive co-sputtering system [15].

for undoped Al_2O_3 layers in this research. A target wafer distance of 15.2 cm (i.e., 6 inch) in combination with a rotation motion of the wafer during deposition were proven to produce the most uniform Al_2O_3 layers [62,63] and they were the settings utilized in all the depositions. A set temperature of 580 °C (i.e., the expected wafer temperature is ~335 °C, based on a calibration measurement with wafer with a bonded thermocouple) and a process pressure of ~4 mTorr (i.e., 0.53 Pa) were used for all depositions.

The bias voltage between the target (cathode) and the chamber (anode) is monitored and it gives an indication of the degree of oxidation of the target. Prior to each deposition and with the substrate still in the load-lock chamber, the bias voltage as a function of oxygen flow is measured using the same gas and power settings as during the deposition and with the shutter of the target open, to determine the desired operating O_2 flow (as it will be discussed in detail in the following sections). During the measurement of the bias curve, it is important to ensure that the bias voltage is stable before moving to the next oxygen setting. The substrate is then introduced into the sputtering chamber and the Al-target is pre-sputtered for 10 minutes using the process settings (Table 1) and the selected oxygen flow, with the shutter in front of the target closed. After the 10 minutes of pre-sputtering, the measurement of the bias voltage is stable and it corresponds to the value obtained during the measurement of the bias curve. Pre-sputtering has as goal to ensure having always the same initial deposition conditions. Both the optical properties (i.e., refractive index and propagation losses) as well as the material structure and morphology of the deposited layers were characterized as a function of oxygen flow.

Table 1. Settings for the deposition of optical guiding Al_2O_3 layers

Visualization	Al-target
Power (W)	200
Ar (sccm)	25
O_2 (sccm)	2.0-2.8
Set temperature (°C)[a]	580
Target-wafer distance (cm)	15.2

[a]expected wafer temperature based on a calibration measurement ~335 °C

A prism coupling method (i.e., Metricon 2010/M) is employed to measure the refractive index and thickness of the deposited films using light of a wavelength of 632.8 nm. The propagation

Optical Materials EXPRESS

losses are qualitatively determined, at the same wavelength, by looking at the streak of light travelling in the layers after coupling using the prism coupler. The optical guiding properties are grouped into three categories in this work: optical guiding, lossy guiding and no guiding. The light should propagate for at least 5 cm without noticeable attenuation by eye for the classification 'guiding' (Fig. 2(a)). The layer is classified as 'lossy' if the light streak diminishes within 5 cm propagation length (Fig. 2(b)). If no light streak is observed the layer is classified as 'no guiding' (Fig. 2(c)).

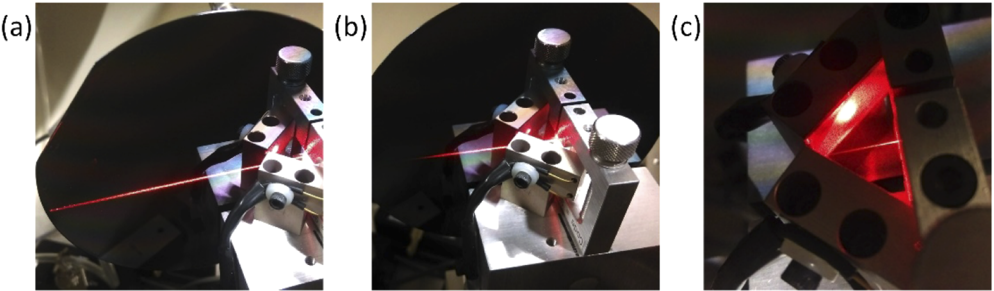

Fig. 2. Examples of the different qualitatively determined classes of guiding. (a) Guiding; (b) On the edge between guiding and lossy guiding; (c) Lossy guiding.

Transmission electron microscopy (TEM) is used to identify the crystalline nature of the layer (i.e., amorphous vs (poly)crystalline) and to estimate the mean crystal size [64,65]. The lamellae for TEM analysis are prepared with the in situ lift-out technique [66] using a focused ion beam (FIB) process (FEI Nova600 NanoLab Dualbeam-SEM/FIB system) and they are mounted on an Omniprobe molybdenum 3-post lift out grid. The lamellae suffer a degree of amorphization during the thinning procedure with the Ga^+ ions. This amorphous layer is reduced to a couple of nanometers during the last stage of the preparation process by milling with subsequently 5 keV and 2 keV acceleration voltage [66]. Small lamellae with a thickness of ~50 nm were prepared with this method. TEM images are made using a Philips CM3000ST-FEG 300 keV TEM system with a Gatan Ultrascan1000 CCD camera with a resolution of ~0.12 nm. The software of the CCD camera is used to make the fast Fourier transform of the TEM image resulting in the diffraction pattern of the structure. This diffraction pattern is used to determine the lattice constant of the (poly)crystalline planes [67].

X-Ray diffraction (XRD) permits to identify the crystalline phase, based on the diffraction footprint of the different phases of Al_2O_3 crystals [55]. The XRD analyses are performed with an X-Ray Powder Diffraction X'Pert-Pro (PANalytical B.V.) with two Cu Kα X-ray sources ($\lambda = 0.15405980$ Å and $\lambda = 0.15444260$ Å). The measurements are done in the Bragg-Bretano θ:θ configuration with a 2θ scan range from 5-100° and a collection time of 48 minutes.

3. Results

3.1. Bias voltage as a function of oxygen flow

The oxygen flow is a crucial parameter in reactive sputtering, influencing the stoichiometry, deposition rate and structure of the deposited Al_2O_3 layers [54,68]. This relationship is often very non-linear and highly complex and the process typically exhibits a hysteresis effect [57].

The bias voltage is measured with the settings described in Section 2, for an increasing and decreasing flow of oxygen, as shown in Fig. 3(a). Our process is free from hysteresis due to the fact that the pump speed (~130 l/s) is large enough to mitigate the influence of the gettering of reactive gas on the target and chamber walls [69]. The total oxygen flow is the sum of all sources

Optical Materials EXPRESS

for reactive gas consumption:

$$Q_{tot} = Q_t + Q_c + Q_p$$

where, Q_t and Q_c are the gettering of O_2 molecules at the target and additional area in the chamber (i.e., substrate and chamber walls) and Q_p is the reactive gas pumped out of the system by the turbomolecular pump. No hysteresis occurs if $dQ_{tot}/dp_{O_2} > 0$ over the whole process region, with p_{O_2} being the partial oxygen pressure. The total pressure is measured using a Baraton pressure gauge (MKS 627B01TCC1B), which has a resolution of 0.1 mTorr. A constant argon flow of 30 sccm is used and the oxygen flow is increased. The partial oxygen pressure is determined by subtraction of the initial pressure ($O_2 = 0$ sccm) from the measured total pressure. A positive linear slope in the relation between the partial oxygen pressure as function of oxygen flow (Fig. 3(b)) indicates that the pump speed is sufficient to fulfill this condition over the whole oxygen flow region presented in this figure, when the settings as mentioned in Table 1 are used [58,70].

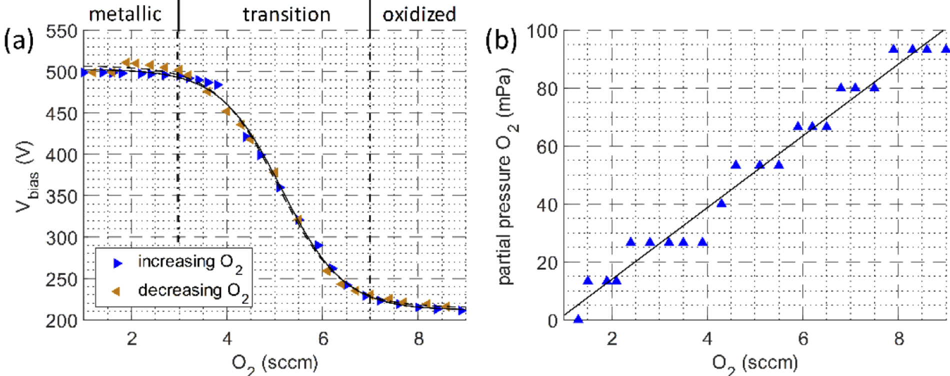

Fig. 3. (a) Bias voltage as function of oxygen flow in the chamber. Three regions are indicated: metallic, transition and oxidized. No hysteresis effect is observed; (b) Partial pressure of oxygen as function of the oxygen flow.

3.2. *Influence of target erosion on process parameters*

The bias curve varies as a function of sputtering target lifetime, as shown in Fig. 4(a). The metallic (V_m) and oxide (V_{ox}) voltages extracted from the bias curve as a function of the number of hours of sputtering of the aluminum target has been plotted in Fig. 4(b). It can be seen that the bias voltage for the metallic target state reduces over time while the bias voltage for the oxidized target state has a much weaker reduction over the lifetime of the target. During the sputtering process, an erosion groove, also known as a racetrack, is formed on the sputtering target above the magnets, which are present to improve the sputter efficiency by increasing the collection of secondary electrons emitted from the target [71]. The reduction of the bias voltage, in general, can be explained by a stronger magnetic field in a deeper racetrack, due to the reduction of the distance to the permanent magnets underneath the target. The stronger magnetic field captures the emitted secondary electrons more efficiently, thereby changing the complex impedance of the target, which leads to a reduction of the bias voltage [71–74]. The decrease in bias voltage is much weaker in the oxidized mode due to an effective smaller increase in the collected emitted electrons. At the same time, the shape of the bias curve also varies, becoming steeper as the lifetime of the target increases (Fig. 3(a)).

The fabrication of optical guiding Al_2O_3 layers with the highest possible deposition rate requires a bias voltage just outside the metallic mode of the target [25,68,75]. We expect,

Optical Materials EXPRESS

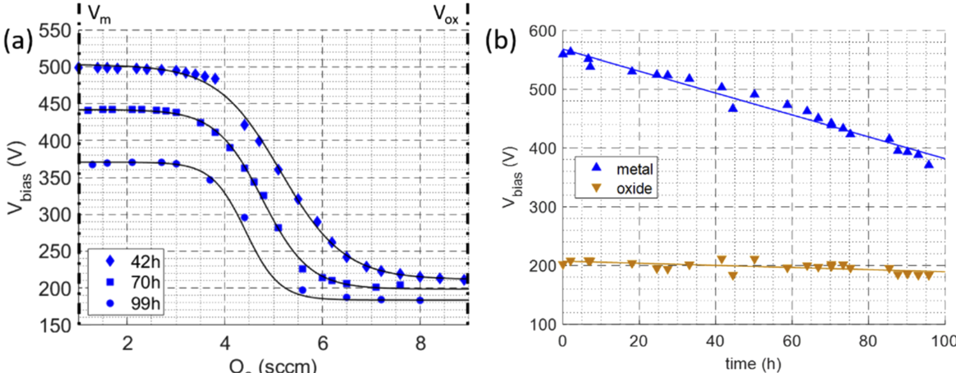

Fig. 4. (a) Bias voltage curve (V_{bias} as a function of O_2 flow) for different moments along the lifetime of the sputtering target (i.e., 42 h, 70 h and 99 h). The sputtering time is net number of hours of sputtering. V_m and V_{ox} are indicated; (b) Evolution of V_m, and V_{ox} over the lifetime of the target.

therefore, that the right process point is related to a certain relative oxidation state of the target. The relative oxidation state of the target can be defined as:

$$\eta_{ox} \equiv \frac{V_m - V_{O_2}}{V_m - V_{ox}}$$

where, V_m and V_{ox} represent the voltage at the metallic and oxidized state of the target, as shown in Fig. 4(a), and V_{O2} defines the bias voltage for a given oxygen flow in the curve [52].

Figure 5(a) shows the relative oxidation of the target as function of oxygen flow with an indication of the three operational modes of the target (i.e., metallic, transition and oxidized). Figure 5(b) shows the oxygen flow necessary to achieve a η_{ox} of 5, 50 and 95% as a function of the number of hours of sputtering from the aluminum target. From this figure it can be seen that the oxygen flow necessary to achieve a $\eta_{ox} = 5\%$ shifts to a higher oxygen value whereas the oxygen flow necessary to achieve $\eta_{ox} = 95\%$ shifts to lower oxygen flow. This is consistent with the change of the shape of the bias curve explained above due to the deepening of the sputtering racetrack (Fig. 4(a)), the narrowing of the transition region being clearly visible in Fig. 5(b).

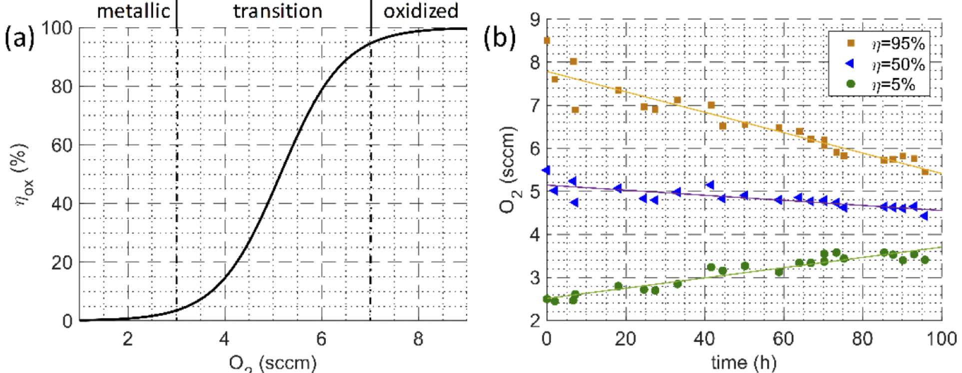

Fig. 5. (a) Relative oxidation state of the target, η_{ox}, as function of oxygen flow; (b) Evolution of the corresponding O_2 flow to achieve a η_{ox} of 5, 50 and 95% as function of lifetime of the target.

Optical Materials EXPRESS

3.3. Influence of the oxidation state of the target on refractive index and propagation losses

The relative oxidation state of the target has a large influence on the refractive index and propagation losses of the sputtered Al_2O_3 layers. To increase our understanding of this influence, a series of Al_2O_3 layers were deposited for several oxidation states of the target, using the parameters of Table 1 for a deposition time of 160 minutes. This deposition time resulted in layers with a thickness between 300 and 750 nm for the different oxidation states, which ensures at least single mode guiding at a wavelength of 633 nm for the thinnest layer. A bias voltage curve as a function of oxygen flow was made, as described in Section 2, for every other deposition to recalibrate the relative oxidation state of the target as a function of oxygen flow.

Figure 6(a) shows a section of the bias voltage curves, for different target ages, as a function of oxygen flow, where the oxygen settings and qualitative optical guiding properties as defined in Section 2 are indicated. From this graph, it can clearly be seen that there is no single value of the bias voltage that always resulted in optical guiding layers. On the other hand, the relative oxidation state appears as a promising parameter to determine the set point for the oxygen flow to obtain optical guiding layers, as shown in Fig. 6(b). All the optical guiding layers in undoped Al_2O_3 deposited using the parameters of Table 1 were obtained at a relative oxidation state of the target of $5 \pm 1.5\%$, for an investigated lifetime of the target as high as 36.2 h.

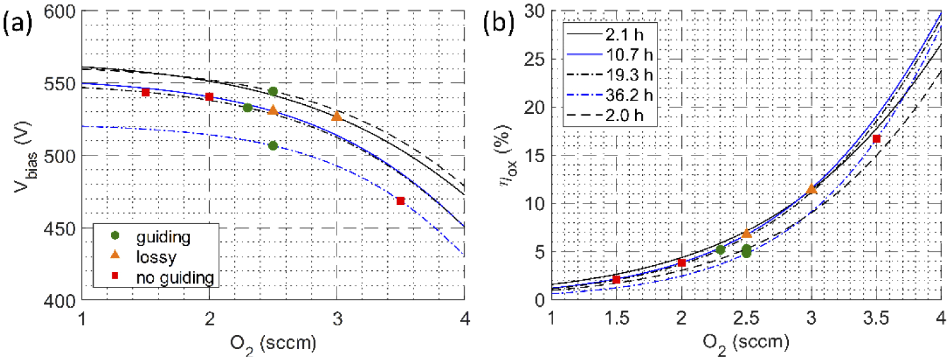

Fig. 6. (a) Section of the bias voltage curve as function of oxygen flow; (b) Relative oxidation state of the target as function of oxygen flow. In both graphs deposition parameters with their optical guiding properties are indicated.

The refractive indices of the guiding layers varied in the range from 1.665 to 1.670 as shown in Fig. 7. The Al_2O_3 layers became lossy for $n > 1.685$. Those losses are attributed to Al_2O_3 crystallites in the layer. Lack of guiding was observed for layers with a $n < 1.665$ (η_{ox} roughly < 5%) or a $n > 1.720$ (η_{ox} roughly > 15%). We believe that the losses in the low refractive index layers are caused by absorption due to aluminum ions, which are not fully oxidized. For layers deposited with a high oxidation state of the target, a refractive index close to that of sapphire ($n \approx 1.766$ at 632.8 nm [6]), the stable crystalline form of Al_2O_3, was obtained. This suggests a high degree of polycrystallinity in the layer, which causes high propagation losses for the deposition settings indicated in Table 1.

To confirm this hypothesis, two samples were prepared, one with low refractive index and good propagation losses and the second one with a high refractive index and high propagation losses. The refractive index was varied by changing the oxygen flow with the aim of working at a different relative target oxidation state of the target. All the other deposition settings are shown in Table 1. Deposition time was 160 min. Table 2 summarizes the deposition and optical characteristics of the two undoped Al_2O_3 layers.

Optical Materials EXPRESS

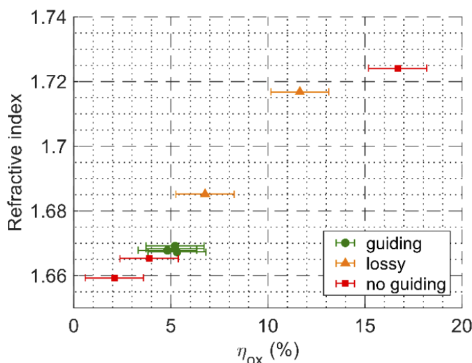

Fig. 7. Refractive index (measured at a wavelength of 632.8 nm using a prism coupler setup) as function of the target oxidation state (error margin of refractive index is 0.001) for undoped Al_2O_3 layers.

Table 2. Characteristics of undoped Al_2O_3 layers used for TEM and XRD

Sample	η_{ox} (%)	n (λ = 632.8 nm)	Deposition rate (nm/min)	Guiding
1	5.2	1.669	3.3	Yes
2	11.6	1.717	2.0	No

The TEM images of the samples 1-2 are shown in Fig. 8(a-b) respectively, with their corresponding diffraction patterns. The predominantly amorphous nature of the Al_2O_3 layers is visible in all the samples in their diffraction pattern (i.e., hazy spot at the center of the diffraction pattern). An additional polycrystalline structure is visible, which is more prominent at a higher relative oxidation state of the target. The lattice spacing of the three rings present in those two samples are inferred from the diffractogram. The spacings are 1.39 Å, 1.97 Å and 2.39 Å, indicated with respectively 1, 2 and 3 in Fig. 8(b). They correspond with the (440), (400) and (311) orientations of γ- Al_2O_3 [76–77].

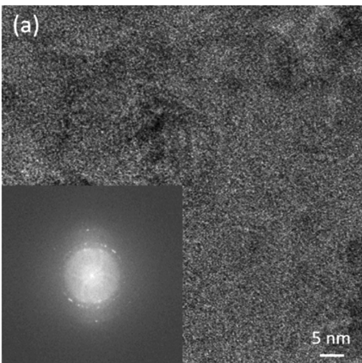

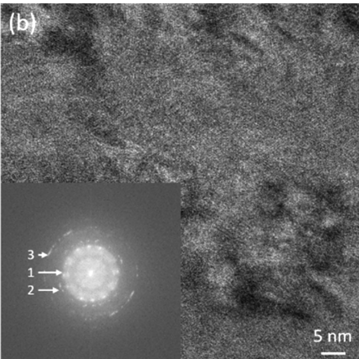

Fig. 8. TEM images and corresponding FFTs (fast Fourier transforms) of: (a) A polycrystalline Al_2O_3 layer with optical guiding (Sample 1 in Table 2); (b) A polycrystalline Al_2O_3 layer without optical guiding (Sample 2 of Table 2).

The XRD results are shown in Fig. 9. The two sharp peaks at 2θ ∼ 33° and 69° correspond to the (002) and (004) peaks of the silicon substrate, respectively. The amorphous network of both Al_2O_3 layers is characterized by the broad halo at the diffraction angle range 2θ ∼ 15-25°. The halo at 2θ ∼ 45° is associated to certain degree of polycrystallinity in the Al_2O_3 layer with

Optical Materials EXPRESS

a refractive index of 1.718. The phase of the crystallization cannot be identified because γ, δ and α Al_2O_3 all have a diffraction peak around 45° [55] and no other halos or peaks have been measured to associate the crystalline phase to the fingerprint peaks as defined in the JCPDS (Joint Committee on Powder Diffraction Standards) charts.

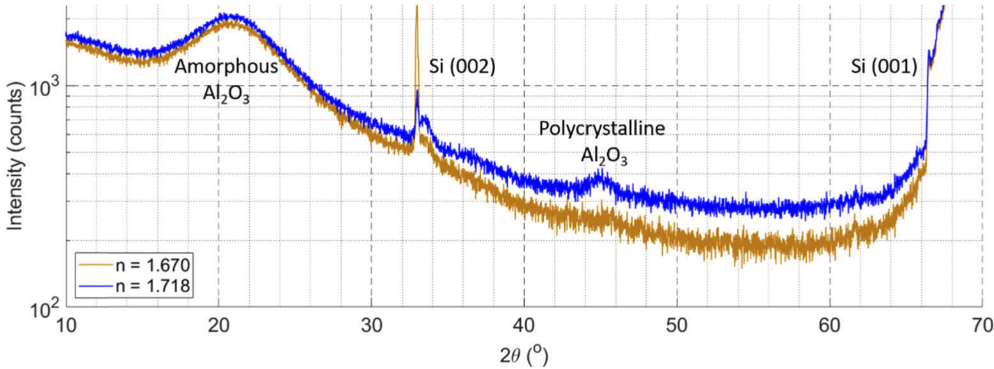

Fig. 9. XRD measurement of two Al_2O_3 layers made with different oxygen concentrations resulting in (a) a guiding layer with n = 1.670 (yellow) and (b) non-guiding layer with n = 1.718 (blue) at 632.8 nm. The blue curve has been shifted 100 counts upwards.

Both TEM and XRD analyses show the dominant amorphous character of the Al_2O_3 network. A degree of polycrystallinity is observed for the high refractive ($n > 1.70$) index layers. The diffraction patterns obtained with TEM indicate, most likely, the presence of polycrystalline γ-Al_2O_3.

The increase in crystallinity due to larger oxygen flow has also been seen for Al_2O_3 coatings [2,50]. The formation of crystalline structure is governed by the diffusion length of the deposited particles and their energetic contribution. The diffusion length is given by the relation $x \sim \sqrt{(D_s/d)}$ where, d, is the deposition rate and $D_s \sim \exp(-1/T_w)$ is the surface diffusion coefficient, which depends on the wafer temperature, T_w [50]. Furthermore, it is hypothesized that sputtering of an oxidized target leads to sputtering of O^- ions, which are accelerated to the surface of the substrate and increase the energy available to the Al and O atoms to react and crystallize in various crystalline structures. Magden *et. al.* reduced the degree of nanocrystallinity of the layer by reducing the substrate temperature and optimizing a bias voltage applied to the substrate [25]. Further research is however needed to identify operational relative oxidation states of the target for different wafer temperatures and substrate bias to obtain optically guiding layers.

4. Conclusions

The relative oxidation state of the target is introduced as key parameter to select the correct oxygen flow to deposit in a reproducible manner optical guiding Al_2O_3 layers despite erosion and evolution of the properties of the target during its lifetime. Optical guidance for undoped Al_2O_3 layers with a refractive index of ∼1.665 has been demonstrated for the depositions made at a set temperature of 580 °C. The optical guiding was achieved with relative oxidation state of the target of $\eta_{ox} \approx 5.0 \pm 1.5\%$ for undoped Al_2O_3 layers. TEM measurements revealed a polycrystalline γ-phase in these layers, which became more pronounced with higher oxidation states of the target.

Funding

European Research Council (648978); Stichting voor de Technische Wetenschappen (15360, NWA.ID.17.100).

Optical Materials EXPRESS

Acknowledgments

The authors would like to acknowledge financial support from the European Research Council Consolidator Grant (ERC) (grant project RENOS "Rare-earth doped novel on-chip sources"-648978) and the Dutch Research Council (NWO) with project numbers NWA.ID.17.100 and TTW 15360.

Disclosures

The authors declare no conflicts of interest.

References

1. X. Tang, F. Luo, F. Ou, W. Zhou, D. Zhu, and Z. Huang, "Effects of negative substrate bias voltage on the structure and properties of aluminum oxide films prepared by DC reactive magnetron sputtering," Appl. Surf. Sci. **259**, 448–453 (2012).
2. R. Cremer, K. Reichert, D. Neuschütz, G. Erkens, and T. Leyendecker, "Sputter deposition of crystalline alumina coatings," Surf. Coat. Technol. **163-164**, 157–163 (2003).
3. M. Sridharan, M. Sillassen, J. Bøttiger, J. Chevallier, and H. Birkedal, "Pulsed DC magnetron sputtered Al_2O_3 films and their hardness," Surf. Coat. Technol. **202**(4-7), 920–924 (2007).
4. J. Wang, Y.-H. Yu, S. Lee, and Y.-W. Chung, "Tribological and optical properties of crystalline and amorphous alumina thin films grown by low-temperature reactive magnetron sputter-deposition," Surf. Coat. Technol. **146-147**, 189–194 (2001).
5. C. Grivas, C. Corbari, G. Brambilla, and P. G. Lagoudakis, "Tunable, continuous-wave Ti:sapphire channel waveguide lasers written by femtosecond and picosecond laser pulses," Opt. Lett. **37**(22), 4630 (2012).
6. I. H. Malitson, "Refraction and dispersion of synthetic sapphire," J. Opt. Soc. Am. **52**(12), 1377–1379 (1962).
7. S. H. Waeselmann, C. E. Rüter, D. Kip, C. Kränkel, and G. Huber, "Nd:sapphire channel waveguide laser," Opt. Mater. Express **7**(7), 2361 (2017).
8. J. D. Bradley, R. Stoffer, L. Agazzi, F. Ay, K. Wörhoff, and M. Pollnau, "Integrated $Al_2O_3:Er^{3+}$ ring lasers on silicon with wide wavelength selectivity," Opt. Lett. **35**(1), 73 (2010).
9. M. Belt and D. J. Blumenthal, "Erbium-doped waveguide DBR and DFB laser arrays integrated within an ultra-low-loss Si_3N_4 platform," Opt. Express **22**(9), 10655 (2014).
10. E. S. Hosseini, P. Purnawirman, J. D. B. Bradley, J. Sun, G. Leake, T. N. Adam, D. D. Coolbaugh, and M. R. Watts, "CMOS-compatible 75 mW erbium-doped distributed feedback laser," Opt. Lett. **39**(11), 3106 (2014).
11. S. A. Vázquez-Córdova, M. Dijkstra, E. H. Bernhardi, F. Ay, K. Wörhoff, J. L. Herek, S. M. García-Blanco, and M. Pollnau, "Erbium-doped spiral amplifiers with 20 dB of net gain on silicon," Opt. Express **22**(21), 25993 (2014).
12. N. Li, E. S. Magden, Z. Su, N. Singh, A. Ruocco, M. Xin, M. Byrd, P. T. Callahan, J. D. B. Bradley, C. Baiocco, D. Vermeulen, and M. R. Watts, "Broadband 2-µm emission on silicon chips: monolithically integrated holmium lasers," Opt. Express **26**(3), 2220 (2018).
13. J. Mu, M. Dijkstra, and S. M. Garcia-Blanco, "Resonant coupling for active-passive monolithic integration of Al_2O_3 and Si_3N_4," IEEE Photonics Technol. Lett. **31**(10), 771–774 (2019).
14. M. de Goede, M. Dijkstra, R. Obregón, J. Ramón-Azcón, E. Martínez, L. Padilla, F. Mitjans, and S. M. Garcia-Blanco, "Al_2O_3 microring resonators for the detection of a cancer biomarker in undiluted urine," Opt. Express **27**(13), 18508 (2019).
15. K. Worhoff, F. Ay, and M. Pollnau, "Optimization of low-loss Al_2O_3 waveguide fabrication for application in active integrated optical devices," ECS Trans. **3**, 17–26 (2006).
16. E. R. Dobrovinskaya, L. A. Lytvynov, and V. Pishchik, *Sapphire Material, Manufacturing, Applications* (Springer, 2009).
17. K. Wörhoff, J. D. B. Bradley, F. Ay, D. Geskus, T. P. Blauwendraat, and M. Pollnau, "Reliable low-cost fabrication of low-loss $Al_2O_3:Er^{3+}$ waveguides with 5.4-dB optical gain," IEEE J. Quantum Electron. **45**(5), 454–461 (2009).
18. J. D. B. Bradley, F. Ay, K. Wörhoff, and M. Pollnau, "Fabrication of low-loss channel waveguides in Al_2O_3 and Y_2O_3 layers by inductively coupled plasma reactive ion etching," Appl. Phys. B **89**(2-3), 311–318 (2007).
19. P. G. Kik and A. Polman, "Erbium-doped optical-waveguide amplifiers on silicon," MRS Bull. **23**(4), 48–54 (1998).
20. P. Xing, G. F. R. Chen, X. Zhao, D. K. T. Ng, M. C. Tan, and D. T. H. Tan, "Silicon rich nitride ring resonators for rare – earth doped telecommunications-band amplifiers pumped at the O-band," Sci. Rep. **7**(1), 9101 (2017).
21. L. Agazzi, K. Wörhoff, and M. Pollnau, "Energy-transfer-upconversion models, their applicability and breakdown in the presence of spectroscopically distinct ion classes: A case study in amorphous Al_2O_3: Er^{3+}," J. Phys. Chem. C **117**(13), 6759–6776 (2013).
22. J. Yang, K. van Dalfsen, K. Wörhoff, F. Ay, and M. Pollnau, "High-gain $Al_2O_3:Nd^{3+}$ channel waveguide amplifiers at 880 nm, 1060 nm, and 1330 nm," Appl. Phys. B **101**(1-2), 119–127 (2010).
23. J. D. B. Bradley, E. S. Hosseini, P. Purnawirman, Z. Su, T. N. Adam, G. Leake, D. Coolbaugh, and M. R. Watts, "Monolithic erbium- and ytterbium-doped microring lasers on silicon chips," Opt. Express **22**(10), 12226 (2014).

24. M. de Goede, L. Chang, J. Mu, M. Dijkstra, R. Obregón, E. Martínez, L. Padilla, F. Mitjans, and S. M. Garcia-Blanco, "Al_2O_3:Yb^{3+} integrated microdisk laser label-free biosensor," Opt. Lett. **44**(24), 5937 (2019).
25. E. S. Magden, N. Li, P. Purnawirman, J. D. B. Bradley, N. Singh, A. Ruocco, G. S. Petrich, G. Leake, D. D. Coolbaugh, E. P. Ippen, M. R. Watts, and L. A. Kolodziejski, "Monolithically-integrated distributed feedback laser compatible with CMOS processing," Opt. Express **25**(15), 18058–18065 (2017).
26. N. Li, D. Vermeulen, Z. Su, E. S. Magden, M. Xin, N. Singh, A. Ruocco, J. Notaros, C. V. Poulton, E. Timurdogan, C. Baiocco, and M. R. Watts, "Monolithically integrated erbium-doped tunable laser on a CMOS-compatible silicon photonics platform," Opt. Express **26**(13), 16200 (2018).
27. J. D. B. Bradley, Z. Su, E. S. Magden, N. Li, M. Byrd, P. Purnawirman, T. N. Adam, G. Leake, D. Coolbaugh, and M. R. Watts, "1.8-µm thulium microlasers integrated on silicon," Proc. SPIE **9744**, 9744U (2016).
28. Z. Su, N. Li, E. S. Magden, M. Byrd, P. Purnawirman, T. N. Adam, G. Leake, D. Coolbaugh, J. D. B. Bradley, and M. R. Watts, "Ultra-compact and low-threshold thulium microcavity laser monolithically integrated on silicon," Opt. Lett. **41**(24), 5708 (2016).
29. N. Li, P. Purnawirman, Z. Su, E. S. Magden, P. T. Callahan, K. Shtyrkova, M. Xin, A. Ruocco, C. Baiocco, E. P. Ippen, F. X. Kärtner, J. D. B. Bradley, D. Vermeulen, and M. R. Watts, "High-power thulium lasers on a silicon photonics platform," Opt. Lett. **42**(6), 1181 (2017).
30. J. D. B. Bradley, R. Stoffer, A. Bakker, L. Agazzi, F. Ay, K. Wörhoff, and M. Pollnau, "Integrated Al_2O_3:Er^{3+} zero-loss optical amplifier and power splitter with 40-nm bandwidth," IEEE Photonics Technol. Lett. **22**(5), 278–280 (2010).
31. J. Rönn, W. Zhang, A. Autere, X. Leroux, L. Pakarinen, C. Alonso-Ramos, A. Säynätjoki, H. Lipsanen, L. Vivien, E. Cassan, and Z. Sun, "Ultra-high on-chip optical gain in erbium-based hybrid slot waveguides," Nat. Commun. **10**(1), 432 (2019).
32. J. Notaros, N. Li, C. V. Poulton, Z. Su, M. J. Byrd, E. S. Magnon, E. Timurdogan, C. Baiocco, N. M. Fahrenkopf, and M. R. Watts, "CMOS-Compatible Optical Phased Array Powered by a Monolithically-Integrated Erbium Laser," J. Lightwave Tech. **37**, 5982–5987 (2019).
33. J. Mu, M. de Goede, M. Dijkstra, and S. M. García-Blanco, "Monolithic integration of Al_2O_3 and Si_3N_4 for double-layer integrated photonic chips," in *Advanced Photonics 2018 (BGPP, IPR, NP, NOMA, Sensors, Networks, SPPCom, SOF)*, 2018, p. ITh1I.1.
34. J. Mu, M. Dijkstra, Y. S. Yong, M. de Goede, L. Chang, and S. M. Garcia Blanco, "Monolithic integration towards double-layer active passive platform," IEEE J. Sel. Top. Quantum Electron. **25**(5), 1–11 (2019).
35. L. Agazzi, J. D. B. Bradley, M. Dijkstra, F. Ay, G. Roelkens, R. Baets, K. Wörhoff, and M. Pollnau, "Monolithic integration of erbium-doped amplifiers with silicon-on-insulator waveguides," Opt. Express **18**(26), 27703 (2010).
36. P. F. Jarschel, M. C. M. M. Souza, R. B. Merlo, and N. C. Frateschi, "Loss compensation in microring-based Si photonics devices via Er^{3+} doped claddings," IEEE Photonics J. **10**(4), 1–12 (2018).
37. P. F. Jarschel and N. C. Frateschi, "Resonant amplification via Er-doped clad Si photonic molecules: Towards compact low-loss/high-Q Si photonic devices," Solid-State Electron. **155**, 144–149 (2019).
38. T. Ishizaka and Y. Kurokawa, "Optical properties of rare-earth ion (Gd^{3+}, Ho^{3+}, Pr^{3+}, Sm^{3+}, Dy^{3+} and Tm^{3+}) -doped alumina films prepared by the sol–gel method," J. Lumin. **92**(1-2), 57–63 (2000).
39. T. Ishizaka, R. Nozaki, and Y. Kurokawa, "Luminescence properties of Tb^{3+} and Eu^{3+}-doped alumina films prepared by sol-gel method under various conditions and sensitized luminescence," J. Phys. Chem. Solids **63**(4), 613–617 (2002).
40. W. Koh, S.-J. Ku, and Y. Kim, "Chemical vapor deposition of Al_2O_3 films using highly volatile single sources," Thin Solid Films **304**(1-2), 222–224 (1997).
41. R. Serna, M. J. de Castro, J. A. Chaos, A. Suarez-Garcia, C. N. Afonso, M. Fernandez, and I. Vickridge, "Photoluminescence performance of pulsed-laser deposited Al_2O_3 thin films with large erbium concentrations," J. Appl. Phys. **90**(10), 5120–5125 (2001).
42. A. Suárez-García, J. Gonzalo, and C. N. Afonso, "Low-loss Al_2O_3 waveguides produced by pulsed laser deposition at room temperature," Appl. Phys. A: Mater. Sci. Process. **77**(6), 779–783 (2003).
43. M. M. Aslan, N. A. Webster, C. L. Byard, M. B. Pereira, C. M. Hayes, R. S. Wiederkehr, and S. B. Mendes, "Low-loss optical waveguides for the near ultra-violet and visible spectral regions with Al_2O_3 thin films from atomic layer deposition," Thin Solid Films **518**(17), 4935–4940 (2010).
44. J. Rönn, L. Karvonen, C. Kauppinen, A. P. Perros, N. Peyghambarian, H. Lipsanen, A. Säynätjoki, and Z. Sun, "Atomic layer engineering of Er-ion distribution in highly doped Er:Al_2O_3 for photoluminescence enhancement," ACS Photonics **3**(11), 2040–2048 (2016).
45. M. Demirtaş, A. Özden, E. Açikbaş, and F. Ay, "Extensive mode mapping and novel polarization filter design for ALD grown Al_2O_3 ridge waveguides," Opt. Quantum Electron. **48**(7), 357 (2016).
46. M. Demirtas, C. Odaci, N. K. Perkgoz, C. Sevik, and F. Ay, "Low loss atomic layer deposited Al_2O_3 waveguides for applications in on-chip optical amplifiers," IEEE J. Sel. Top. Quantum Electron. **24**(4), 1–8 (2018).
47. J. J. Diaz Leon, D. M. Fryauf, J. E. Volk, and N. P. Kobayashi, "Aluminum oxide waveguides for improved transmission in the visible and near-infrared spectrum," IEEE Photonics Technol. Lett. **31**(1), 43–45 (2019).
48. C. J. Kang, J. S. Chun, and W. J. Lee, "Properties of aluminium oxide films prepared by plasma-enhanced metal-organic chemical vapour deposition," Thin Solid Films **189**(1), 161–173 (1990).

49. K. Bobzin, E. Lugscheider, M. Maes, and C. Piñero, "Relation of hardness and oxygen flow of Al_2O_3 coatings deposited by reactive bipolar pulsed magnetron sputtering," Thin Solid Films **494**(1-2), 255–262 (2006).
50. A. Khanna and D. G. Bhat, "Nanocrystalline gamma alumina coatings by inverted cylindrical magnetron sputtering," Surf. Coat. Technol. **201**(1-2), 168–173 (2006).
51. N. D. Madsen, B. H. Christensen, S. Louringa, A. N. Berthelsen, K. P. Almtoft, L. P. Nielsen, and J. Bøttiger, "Controlling the deposition rate during target erosion in reactive pulsed DC magnetron sputter deposition of alumina," Surf. Coat. Technol. **206**(23), 4850–4854 (2012).
52. P. Lei, W. Leroy, B. Dai, J. Zhu, X. Chen, J. Han, and D. Depla, "Study on reactive sputtering of yttrium oxide: Process and thin film properties," Surf. Coat. Technol. **276**, 39–46 (2015).
53. I. Safi, "Recent aspects concerning DC reactive magnetron sputtering of thin films: a review," Surf. Coat. Technol. **127**(2-3), 203–218 (2000).
54. V. Edlmayr, M. Moser, C. Walter, and C. Mitterer, "Thermal stability of sputtered Al_2O_3 coatings," Surf. Coat. Technol. **204**(9-10), 1576–1581 (2010).
55. X. Zhang, J. Zhu, L. Zhang, K. Kishimoto, S. Du, and X. Yin, "Crystallization of alumina films deposited by reactive magnetron sputtering with resputtering technique at low temperature," Surf. Coat. Technol. **228**, S393–S396 (2013).
56. S. Berg, H. Blom, T. Larsson, and C. Nender, "Modeling of reactive sputtering of compound materials," J. Vac. Sci. Technol., A **5**, 202–207 (1987).
57. K. Strijckmans, R. Schelfhout, and D. Depla, "Tutorial: Hysteresis during the reactive magnetron sputtering process," J. Appl. Phys. **124**(24), 241101 (2018).
58. M. K. Smit, G. A. Acket, and C. J. van der Laan, "Al_2O_3 films for integrated optics," Thin Solid Films **138**(2), 171–181 (1986).
59. M. Serényi, T. Lohner, G. Sáfrán, and J. Szívós, "Comparison in formation, optical properties and applicability of DC magnetron and RF sputtered aluminum oxide films," Vacuum **128**, 213–218 (2016).
60. D. B. Keck, R. D. Maurer, and P. C. Schultz, "On the ultimate lower limit of attenuation in glass optical waveguides," Appl. Phys. Lett. **22**(7), 307–309 (1973).
61. S. Dai, C. Yu, G. Zhou, J. Zhang, G. Wang, and L. Hu, "Concentration quenching in erbium-doped tellurite glasses," J. Lumin. **117**(1), 39–45 (2006).
62. C. I. van Emmerik, L. Chang, M. Goede, J. Mu, and S. M. Garcia-Blanco, "Single-layer active-passive Al_2O_3 photonic integration platform," Opt. Mater. Express **8**(10), 3049–3054 (2018).
63. G. Bräuer, "Magnetron Sputtering," Comprehensive Materials Processing **4**, 57–73 (2014).
64. P. J. Goodhew and J. Humphreys, *Electron Microscopy and Analysis*, 3 edit. Taylor & Francis (2001).
65. R. F. Egerton, *Physical Principles of Electron Microscopy* (Springer US, 2006).
66. J. Mayer, L. A. Giannuzzi, T. Kamino, and J. Michael, "TEM Sample Preparation and FIB-Induced Damage," MRS Bull. **32**(5), 400–407 (2007).
67. C. Kittel, *Introduction to Solid State Physics*, 8th ed., vol. 37, no. 11 (John Wiley & Sons, Ltd, 2005).
68. A. G. Spencer, R. P. Howson, and R. W. Lewin, "Pressure stability in reactive magnetron sputtering," Thin Solid Films **158**(1), 141–149 (1988).
69. S. Berg and T. Nyberg, "Fundamental understanding and modeling of reactive sputtering processes," Thin Solid Films **476**(2), 215–230 (2005).
70. E. Särhammar, T. Nyberg, and S. Berg, "Applying 'the upgraded Berg model' to predict hysteresis free reactive sputtering," Surf. Coat. Technol. **290**, 34–38 (2016).
71. D. Depla, K. Strijckmans, and R. De Gryse, "The role of the erosion groove during reactive sputter deposition," Surf. Coat. Technol. **258**, 1011–1015 (2014).
72. D. Depla, S. Heirwegh, S. Mahieu, J. Haemers, and R. De Gryse, "Understanding the discharge voltage behavior during reactive sputtering of oxides," J. Appl. Phys. **101**(1), 013301 (2007).
73. S. Kadlec, J. Musil, and J. Vyskočil, "Modeling of inhomogeneous film deposition and target erosion in reactive sputtering," J. Vac. Sci. Technol., A **8**(3), 1560–1565 (1990).
74. D. Depla, S. Mahieu, and R. De Gryse, "Magnetron sputter deposition: Linking discharge voltage with target properties," Thin Solid Films **517**(9), 2825–2839 (2009).
75. W. D. Sproul, D. J. Christie, and D. C. Carter, "Control of reactive sputtering processes," Thin Solid Films **491**(1-2), 1–17 (2005).
76. R. S. Zhou and R. L. Snyder, "Structures and transformation mechanisms of the η, γ and θ transition aluminas," Acta Crystallogr., Sect. B: Struct. Sci. **47**(5), 617–630 (1991).
77. W. Engelhart, W. Dreher, O. Eibl, and V. Schier, "Deposition of alumina thin film by dual magnetron sputtering: Is it γ-Al_2O_3?" Acta Mater. **59**(20), 7757–7767 (2011).